MNRAS **000**, 1–10 (2019) Preprint 8 May 2020 Compiled using MNRAS LATEX style file v3.0

# ON THE GEOMETRY OF THE X-RAY EMISSION FROM PULSARS
## A Consistent Inclination and Beaming Solution for the Be/X-ray Pulsar SXP 1062

R. C. Cappallo,[1,2]⋆ S. G. T. Laycock,[1,2] D. M. Christodoulou,[2,3]
A. Roy,[1,2] S. Bhattacharya,[1,2] M. J. Coe,[4] and A. Zezas[5,6]

[1] *Department of Physics and Applied Physics, University of Massachusetts Lowell, Lowell MA, 01854, USA*
[2] *Lowell Center for Space Science and Technology, 600 Suffolk Street, Lowell MA, 01854, USA*
[3] *Department of Mathematical Sciences, University of Massachusetts Lowell, Lowell MA, 01854, USA*
[4] *School of Physics and Astronomy, Southampton University, Highfield, Southampton, SO17 1BJ, UK*
[5] *Physics Department & Institute of Theoretical & Computational Physics, University of Crete, 71003 Heraklion, Crete, Greece*
[6] *Harvard-Smithsonian Center for Astrophysics, 60 Garden Street, Cambridge MA, 02138, USA*

Accepted XXX. Received YYY; in original form ZZZ

**ABSTRACT**

SXP 1062 is a long-period X-ray pulsar with a Be optical companion located in the Small Magellanic Cloud. First discovered in 2010 from *XMM-Newton* data, it has been the target of multiple observational campaigns due to the seeming incongruity between its long spin period and recent birth. In our continuing modelling efforts to determine the inclination angle ($i$) and magnetic axis angle ($\theta$) of X-ray pulsars, we have fitted 19 pulse profiles from SXP 1062 with our pulsar model, *Polestar*, including three consecutive *Chandra* observations taken during the trailing end of a Type I outburst. These fittings have resulted in most-likely values of $i = 76° \pm 2°$ and $\theta = 40° \pm 9°$. SXP 1062 mostly displays a stable double-peaked pulse profile with the peaks separated by roughly a third of a phase, but recently the pulsar has spun up and widened to a spacing of roughly half of a phase, yet the *Polestar* fits for $i$ and $\theta$ remain constant. Additionally we note a possible correlation between the X-ray luminosity and the separation of the peaks in the pulse profiles corresponding to the highest-luminosity states.

**Key words:** accretion, accretion disks – methods: numerical – stars: magnetic field – stars: neutron – pulsars: general – X-rays: binaries

## 1 INTRODUCTION

X-ray pulsars (XRPs) are some of the most prolific producers of X-rays in the observable universe. These objects are neutron stars (NSs) residing in a binary system with an optical companion. In this type of High-mass X-ray binary (HMXB) system, the optical counterpart donates material to the NS via a circumstellar disk or a strong stellar wind (Walter et al. 2015). Some of this hydrogen-rich material is gravitationally bound to the NS. As it approaches the NS surface it is ionized and, accelerated by gravity, the plasma follows the NS's magnetic field lines (Basko & Sunyaev 1976). During this acceleration gravitational potential energy is exchanged for kinetic energy, resulting in the radiation of energetic photons. These photons are often directed preferentially along the magnetic dipole axis due to a geometrical collimation effect (Christodoulou et al. 2018). The rotation of the NS coupled with misaligned magnetic and spin axes produces observable periodic pulsations.

The focus of this paper is the X-ray bright source SXP 1062, a Be/X-ray binary (BeXRB) pulsar in the Small Magellanic Cloud (SMC). BeXRBs are the most prevalent subclass of HMXBs, comprising 70% and 90% of galactic and SMC HMXBs respectively (Paul & Naik 2011; Coe & Kirk 2015a). In these systems the donor stars are Be stars

⋆ E-mail: rigelcappallo@gmail.com

which display emission lines in their optical spectrum owing to large circumstellar disks (Porter & Rivinius 2003). These disks supply material to the pulsar and may be truncated through tidal interaction (Reig 2011). Recently Brown et al. (2019) have performed smoothed particle hydrodynamic (SPH) simulations supporting observational evidence that the size of the circumstellar disk is governed by the orbital period and size of the semi-major axis.

In an XRP the area near the magnetic poles of the NS is rich in complexity. The in-falling material from the accretion disk is being simultaneously accelerated and compressed as it nears the NS surface, where magnetic field lines converge. Upon reaching the NS surface a mound is formed that emits thermally with a black-body spectrum (Becker & Wolff 2007). If enough material is supplied the thermal radiation from the mound begins to form a shock as it meets the in-falling matter. This shock rises further from the NS surface and underneath an accretion column begins to form (Basko & Sunyaev 1976).

The formation and growth of these accretion columns is governed by the struggle between gravity and radiation pressure. In the sub-critical regime the accretion stream is decelerated by thermal electrons through Coulomb forces. In the super-critical regime a shock is formed with the resulting accretion column below. There is a critical luminosity ($L_{X,crit}$), specific to each source and dependent on the magnetic field and compactness of the NS, that divides these two regimes (Becker et al. 2012).

This critical luminosity marks the point where the dominant orientation of the emitted radiation begins to change. For $L_X < L_{X,crit}$ there exists a "pencil-beam" component which consists of radiation directed along the local magnetic magnetic field lines (Zavlin et al. 1995), while for $L_X \geq L_{X,crit}$ a "fan-beam" component begins to emerge which exhibits maximum radiation perpendicular to the magnetic dipole axis (Schönherr et al. 2007).

We have extracted light curves from archival *Chandra*, *XMM-Newton*, and *NuSTAR* observations and have used our geometric model *Polestar* (Cappallo et al. 2017, 2019) in order to produce individual fits to 19 unique pulse profiles (see Table 1 for the ObsIDs and observation dates corresponding to these profiles). We have performed a statistical analysis of the results in an attempt to find the best-fit geometric parameters of the pulsar and the orientation of its magnetic dipole axis relative to its spin axis. In addition, we have explored the changes in the model fits for three consecutive *Chandra* observations occurring at the tail end of a Type I outburst[1] and have examined changes in profiles found in the highest luminosity states.

In the following sections, we describe the analysis of the data set and the statistics of the results. § 2 is a recap of the literature on this system. In § 3 we describe the data used in this study. In § 4 and § 5 we provide a brief description of the fitting procedure and a detailed analysis of the fits, followed by a discussion and our conclusions in § 6 and § 7, respectively.

[1] These are periodic events that coincide with periastron passage of the NS (see, e.g. Reig & Nespoli 2013, and references therein).

## 2 SXP 1062

SXP 1062 is located at RA=01:27:45.9 and Dec=-73°32′56″.3. There have been three Type I outbursts observed which, along with optical data, have constrained the orbital period ($P_{orb}$) for this system to 668 ± 10 days (Gonzales-Galan et al. 2017). The orbital eccentricity is low for a NS BeXRB, given as $e \leq 0.2$, with the orbital inclination angle calculated to be 73° ± 2° by Serim et al. (2017), utilizing a pulse-arrival timing technique from multiple *SWIFT* observations.

### 2.1 X-ray Source

CXO J012745.97-733256.5 (SXP 1062) was discovered with a spin period ($P_{spin}$) of 1062 s in 2010 using both *Chandra* ACIS-I and *XMM-Newton* EPIC-pn data while observing the star-forming region NGC 602 in the eastern region of the SMC wing (Henault-Brunet et al. 2012). It has been reported to vary in X-ray luminosity by approximately one order of magnitude, with a range of $L_{X,min} = 5.4 \pm 0.1 \times 10^{35}$ erg s$^{-1}$ to $L_{X,max} = 3.0 \pm 0.1 \times 10^{36}$ erg s$^{-1}$(Gonzales-Galan et al. 2017). This nominal variability in X-ray luminosity and lack of any null observations, coupled with a $P_{spin} > 200$ s and a $P_{orb} > 200$ d, classify SXP 1062 as a persistent BeXRB (Reig & Roche 1999).

### 2.2 Optical Counterpart

The optical counterpart of SXP 1062 is the Be star 2dFS 3831 (Evans et al. 2004), with a classification of B0-0.5III and a mass of ∼ 15 $M_\odot$(Henault-Brunet et al. 2012). Gonzales-Galan et al. (2017) noted optical variation on the order of ∼ 0.6 mag in archival SALT and OGLE data. The first two optical outbursts suggested $P_{orb} \simeq 656 \pm 2$ days (Schmidtke et al. 2012), with further confirmation due to the fast rise and exponential decay of these outbursts, as noted by Strum et al. (2013). Subsequently Gonzales-Galan et al. (2017) refined $P_{orb}$ to 668 ± 10 days. The H$\alpha$ line profiles indicate that the inclination angle of the circumstellar disk is large (i.e. it is oriented closer to face-on), while the X-ray spectral fitting suggests that the NS orbit may not lie in the same plane as this disk (Gonzales-Galan et al. 2017).

### 2.3 Associated Supernova Remnant

Since its discovery SXP 1062 has been the subject of much interest as it was the first BeXRB to be associated with a parent supernova remnant (SNR, Fig. 1, Gonzales-Galan et al. (2017)). MC-SNR J0127-7332 was discovered in H$\alpha$ and OIII filter images by Henault-Brunet et al. (2012). This is unexpected as standard theory predicts any parent SNR will have faded beyond detectability before accretion onto the associated NS begins (Lipunov 1992). Another remarkable fact is that the calculated kinetic age of the SNR (∼ 20 kyr) seems to put an upper limit on the age of the pulsar that is incongruous with current theory (i.e.

**Figure 1.** A composite image of SXP 1062 and its associated SNR combining optical data from the Cerro Tololo Inter-American Observatory (colored red and green) with X-ray data from both *Chandra* and *XMM-Newton* (colored blue). SXP 1062 is the bright blue object to the right with the parent SNR surrounding it. Image courtesy of NASA.

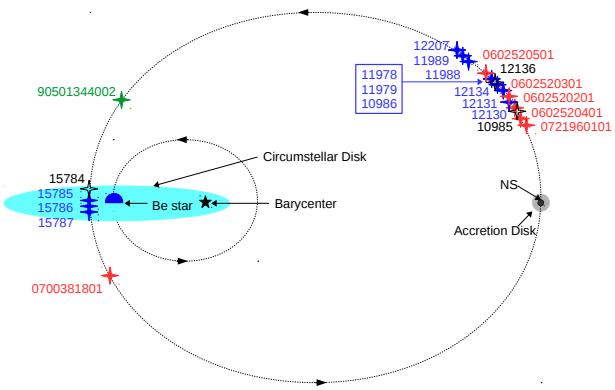


**Figure 2.** A diagram (not to scale) of the SXP 1062 system at apastron. The orbital positions of the NS when the 19 observations used in this study occurred are denoted by a four-pointed star accompanied by the corresponding ObsID, with *Chandra* in blue, *XMM-Newton* in red, and *NuSTAR* in green. The empty black stars (with corresponding black ObsIDs) are the three *Chandra* observations where the source was detected, but significant pulsations were not. The plane of the cirumstellar disk is nearly orthogonal to the orbital plane, as discussed in § 6. The orbital period for this system is 668 ± 10 days.

the pulse period is too long to have been born in the ms range and spun down to $P_{spin} > 1000$ s through proposed theoretical mechanisms (Popov & Turolla 2012)).

Multiple possible explanations for this seeming incongruity are found in the literature. Haberl et al. (2012) suggested this X-ray pulsar was born rotating unusually slowly, with 0.5 sec given as a lower limit. Popov & Turolla (2012) and Fu & Li (2012) independently put forward the possibility that this source is an accreting magnetar (with $B > 10^{14}$ G). If this were the case, then magnetic breaking and field dissipation could result in the long $P_{spin}$ combined with the high $\dot{P}$. Ikhsanov (2012) refined this idea, suggesting a source with a slightly weaker magnetic field ($B \simeq 5 \times 10^{13}$ *G*) which is accreting magnetized material, achieving the required $\dot{P}$ through magnetic torques.

In support of these hypotheses Klus et al. (2014) predicted that longer period pulsars in BeXRBs should have much larger magnetic fields than the assumed canonical value of $\sim 10^{12}$ G, while other sources suggest the required $\dot{P}$ can still occur in sources with $B \leq 10^{12}$ G (see, e.g. Christodoulou et al. 2018).

## 3 OBSERVATIONS AND DATA REDUCTION

In this study 19 pulse profiles were analyzed from *Chandra*, *XMM-Newton*, and *NuSTAR* archival data with observation dates ranging from MJD 55280 to 58780 (March 2010 to October 2019). Source-specific light curves were extracted from a universal energy range of 3 to 10 keV and then folded on the periods found from a Lomb-Scargle periodogram analysis (Lomb 1976; Scargle 1982) with detections at $s \geq 99\%$ significance, following the same data-reduction prescription and timing analysis as described in Cappallo et al. (2019). All observations used in this study are given in Table 1 and occurred at different points in the ephemeris, as presented in Fig. 2.

## 4 FITTING STRATEGY

*Polestar* (Cappallo et al. 2017) is a geometric model of an accreting XRP with parameters defining the hot-spot locations along with the geometry of each emission region, incorporating both fan and pencil-beam components (e.g. Zavlin et al. 1995). Each of these parameters may be varied or kept fixed when fitting folded profiles. In this work, the data were fitted with an antipodal hot-spot arrangement (two hot spots oriented along a single magnetic dipole axis passing through the center of the NS). For a visualization of *Polestar's* geometry see Fig. 3.

We followed the same prescription laid out in § 4.2 of Cappallo et al. (2019) for the fitting performed in this paper. Briefly stated, each profile was fit with an antipodal, 6-parameter version of *Polestar* where the inclination angle ($0° \leq i \leq 90°$), the angle of the primary hot spot ($0° \leq \theta \leq 90°$), the longitude ($0° \leq \phi \leq 360°$), the power of the cosine emission function ($1 \leq P_{cos} \leq 9$), the power of the sine emission function ($1 \leq P_{sin} \leq 9$), and the contribution from the two functions to the overall emission ($0 \leq P_{rat} \leq 1$,

**Table 1.** SXP 1062 Observations with Detected Pulsations

| ObsID | MJD | Period | Lx | PF | Exp Time | Tel./Array |
|---|---|---|---|---|---|---|
| 0602520401 | 55280 | 1060.9 | 3.57 | 0.35 | 63.76 | XMM/tot |
| 0602520201 | 55286 | 1062.7 | 4.05 | 0.34 | 110.25 | XMM/pn |
| 12130 | 55287 | 1055.9 | 4.42 | 0.29 | 27.44 | CH/I |
| 0602520301 | 55288 | 1062.7 | 4.03 | 0.28 | 91.16 | XMM/tot |
| 12131 | 55288 | 1062.9 | 4.00 | 0.38 | 28.48 | CH/I |
| 12134 | 55291 | 1062.9 | 3.90 | 0.40 | 34.75 | CH/I |
| 10986 | 55293 | 1060.6 | 4.50 | 0.36 | 36.88 | CH/I |
| 11979 | 55296 | 1062.4 | 4.69 | 0.30 | 38.92 | CH/I |
| 11978 | 55298 | 1060.6 | 4.93 | 0.28 | 34.49 | CH/I |
| 0602520501 | 55298 | 1060.0 | 3.04 | 0.33 | 45.74 | XMM/pn |
| 11988 | 55312 | 1059.9 | 4.34 | 0.32 | 36.37 | CH/I |
| 11989 | 55313 | 1062.1 | 4.01 | 0.36 | 29.95 | CH/I |
| 12207 | 55315 | 1069.8 | 3.57 | 0.49 | 20.11 | CH/I |
| 0700381801 | 56214 | 1064.4 | 19.99 | 0.13 | 29.87 | XMM/tot |
| 0721960101 | 56576 | 1073.2 | 3.23 | 0.24 | 75.89 | XMM/tot |
| 15785 | 56837 | 1085.4 | 15.44 | 0.23 | 31.03 | CH/I |
| 15786 | 56846 | 1081.2 | 13.08 | 0.27 | 30.71 | CH/I |
| 15787 | 56856 | 1085.5 | 9.83 | 0.21 | 29.09 | CH/I |
| 90501344002 | 58780 | 980.2 | 42.00 | 0.53 | 40.41 | NuSTAR |

Observations of SXP 1062 fitted with *Polestar*. The period is reported in seconds, X-ray luminosity is calculated assuming a distance to the SMC of 62 ± 3 kpc (Haschke, Grebel, & Duffau 2012) and is given in units of $10^{35}$ erg $s^{-1}$, the pulsed fraction (PF) is calculated following equation A given in § A, exposure time is in units of ksec, CH/I represtents the *Chandra* ACIS-I array, XMM/pn represents the *XMM-Newton* EPIC-pn detector, XMM/tot represents a summed contribution from the *XMM-Newton* EPIC-pn, MOS1, and MOS2 detectors, and NuSTAR represents a summed contribution from both of *NuSTAR*'s A and B detectors.

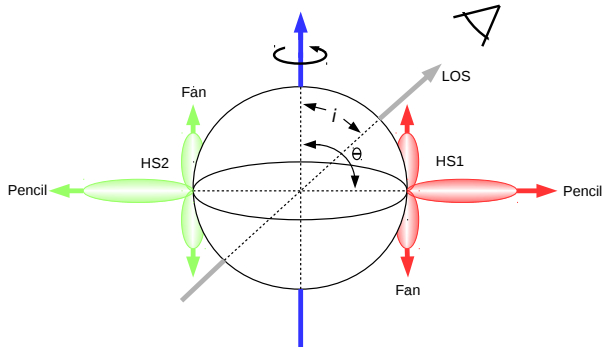


**Figure 3.** A diagram of the underlying geometry of *Polestar*. The blue arrow represents the angular momentum vector (i.e. the NS spin axis), the grey vector points in the direction of the line of sight (LOS), and the red and green hot spot (HS) vectors match the red and green components displayed in the pulse profile fits (Figs. 4, 6, 8, & 10).

with 0 representing exclusively fan emission and 1 representing exclusively pencil emission) were each allowed to vary. Once a most-likely value of the inclination angle $i$ was determined, a final iteration of fitting was performed with $i$ fixed at the most-likely value ± $\sigma_i$[2].

[2] This final fitting with $i$ fixed is performed since, physically speaking, the inclination angle is not expected to vary appreciably throughout observations.

## 5 MODEL ANALYSIS AND RESULTS

For a detailed description of *Polestar*, see both Cappallo et al. (2017) & Cappallo et al. (2019).

### 5.1 Six-Parameter Fit

After the inital 6-parameter *Polestar* fit was performed on each pulse profile a preferred orientation for SXP 1062 emerged. An example profile with the accompanying *Polestar* fit is given in Fig. 4. This particular profile has a double-peaked structure, with the peaks separated by ∼ 0.3 Φ. This appears to be a signature of this source, as the majority of the profiles in this study share this characteristic. However, sometimes a third, much smaller peak is also visible. In order to accommodate this signature coupled with a relatively low pulsed fraction, the *Polestar* fitting strongly prefers values of $i > 60°$, which implies that the primary HS is always visible as well as allowing the secondary HS to be visible for a large fraction of each revolution. Additionally, a small fan (i.e. sine) contribution in the emission geometry is required to obtain two peaks separated by ∼ 0.3 Φ, as an antipodal arrangement coupled with exclusively pencil (i.e. cosine) emission can only produce peaks separated by ∼ 0.5 Φ.

The distribution of the values of the inclination angle in the 6-parameter *Polestar* fits for SXP 1062 is roughly gaussian, with a mean value of $\mu_i = 75°$ and a standard deviation ($\sigma_i$) of 6°, while the $\theta$ distribution has a mean of $\mu_\theta = 41°$ with $\sigma_\theta = 10°$ (Fig. 5).

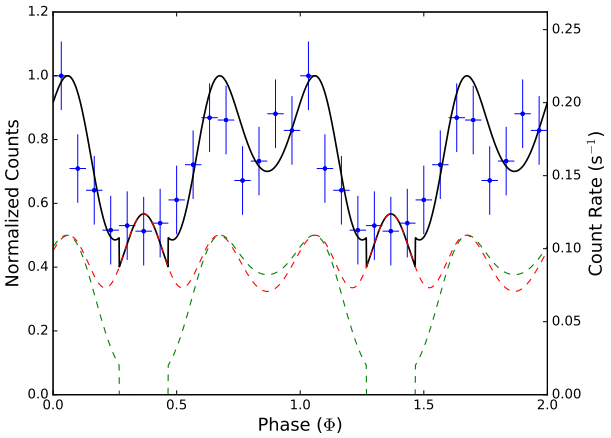


**Figure 4.** An example pre-outburst profile with the corresponding *Polestar* fit from *XMM-Newton* (ObsID 0602520301). The blue points are the data with associated error and bin-size, the red and green dashed lines are the contribution from each individual HS, and the solid black line is the total emission from the model. This profile displays two peaks per phase, separated by $\sim$ 0.3 Φ, which is a common characteristic of many SXP 1062 pulse profiles.

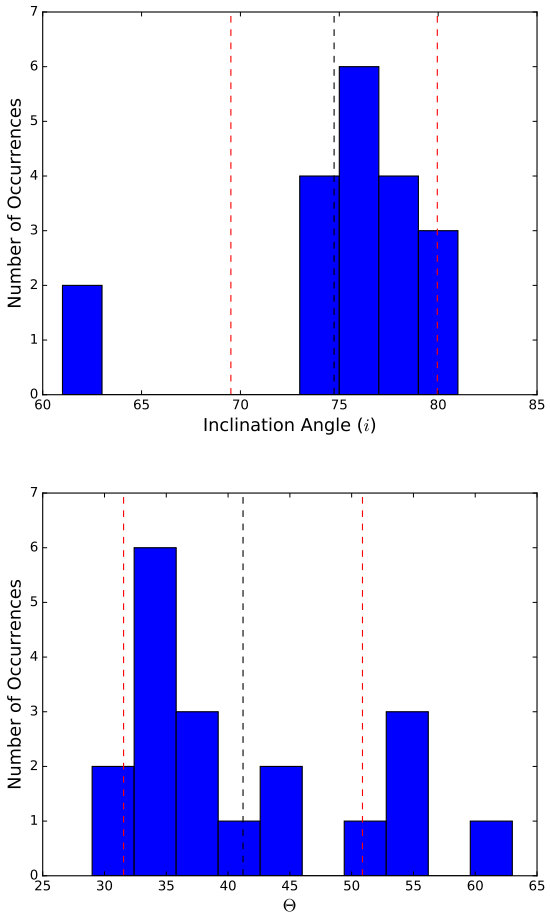


**Figure 5.** Histograms for the inclination angle ($i$, *top*) and the angle between the spin and magnetic dipole axes ($\theta$, *bottom*) for the 19 individual *Polestar* fits for SXP 1062. The vertical black-dashed lines represent the mean ($\mu$) of the distributions ($\mu_i = 75°$, $\mu_\theta = 41°$), and the vertical red-dashed lines are one standard deviation ($\sigma_i$, $\sigma_\theta$) from the mean.

### 5.2 Fitting the 2014 Outburst

Fig. 6 shows a sequence of three *Polestar* fits from the tail end of the Type I outburst that was captured by the *Chandra* ACIS-I array in July of 2014 (ObsIDs 15785 to 15787). These three observations spanned 19 days over the course of which the luminosity steadily decreased from 15.4 $\times$ $10^{35}$ erg s$^{-1}$ to 9.8 $\times$ $10^{35}$ erg s$^{-1}$. Spectral analysis of these observations by Gonzales-Galan et al. (2017) shows no appreciable change in the spectral profile aside from the expected spectrum-wide decrease in count-rate.

There was a preceding observation (ObsID 15784) with substantially less X-ray flux and no significant pulsations detected. The relatively low flux of this observation was likely due to an increase in the absorbing column occurring just before periastron passage as the NS was shielded by the circumstellar disk of the mass donor (Gonzales-Galan et al. 2017). This effect is discussed in greater detail in § 6.

All three profiles from this outburst are triple-peaked, with two prominent peaks at $\Phi \simeq 0.05$ and $\Phi \simeq 0.78$ and a much smaller peak at $\Phi \simeq 0.5$. The *Polestar* fits for each profile in Fig. 6 also share a triple-peaked structure, although the constraint of an antipodal magnetic dipole with six free parameters does not allow ideal fitting of the peak magnitudes.

Using a kernel density estimation (KDE) technique we generated pulse profiles and then stacked them to study changes in the pattern (Fig. 7). Unlike binned profiles, KDE permits bias-free determination of the peak locations (Laycock 2003). In addition to the expected decrease in overall count rate, the first peak (at $\Phi \simeq 0.78$), which was the strongest peak at high $L_X$, diminishes as the outburst subsides. This phenomenon can be seen in the binned data points in the three panels of Fig. 6 as well. The spacing between the two peaks also changed between observations, which is discussed in §§ 5.4 & 6.

### 5.3 The 2019 *NuSTAR* Observation: A Recent Spin-up Event

*NuSTAR* observed SXP 1062 near the end of October in 2019, more than five years after the last *Chandra* or *XMM-Newton* observation. Many of the system's attributes had changed dramatically over that time. The X-ray luminosity from 3 to 10 keV was the highest ever recorded by a factor of two ($L_X = 4.2 \times 10^{36}$ erg s$^{-1}$), the pulsed fraction was at a maximum for this source (0.53, Table 1), and the period had decreased by $\sim$ 100 s.

Collectively these facts point to a significant shift in the system, perhaps associated with the possible glitch

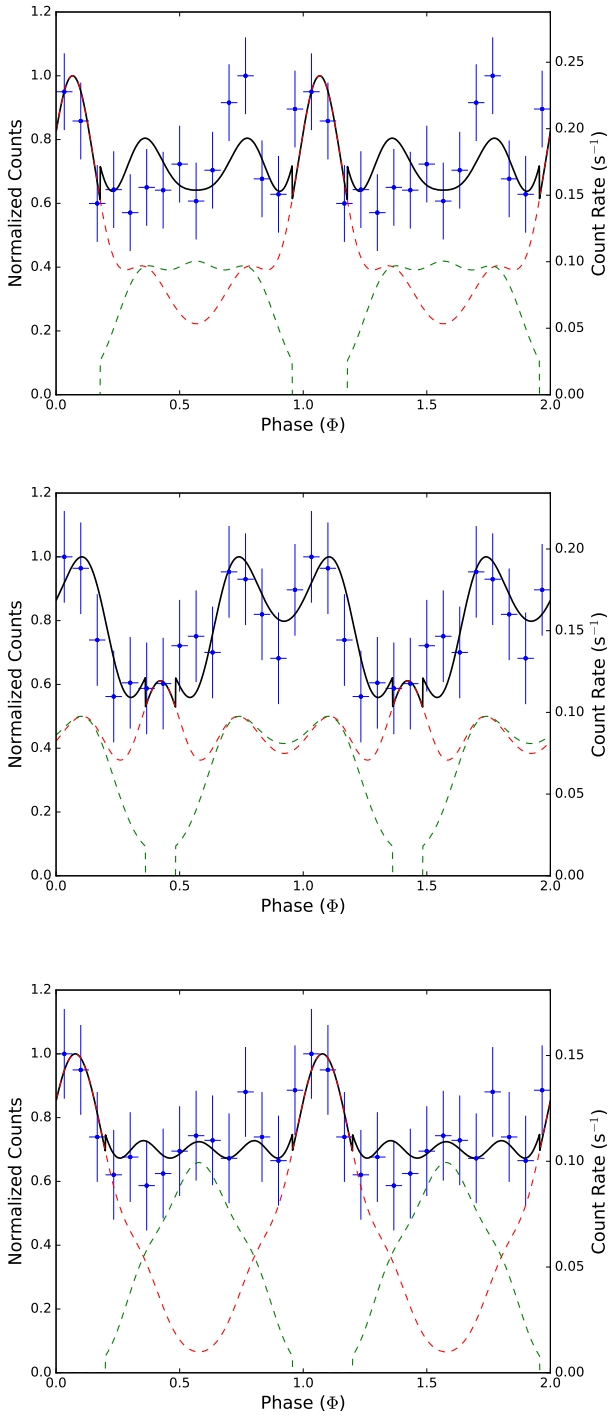


**Figure 6.** The evolution of the pulse profile and the corresponding *Polestar* fits at the tail end of SXP 1062's second outburst (from the top: *Chandra* ObsIDs 15785, 15786, & 15787). Note that the small dip present at the peak in the highest luminosity profile gradually disappears. In these three panels luminosity decreases from top to bottom.

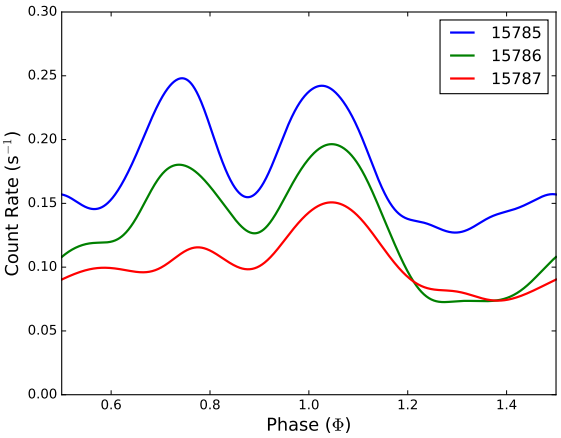


**Figure 7.** Stacked pulse profiles from three *Chandra* observations at the tail end of the 2014 Type I outburst. These smoothed profiles were created from the binned profiles using a kernel density estimator; they correspond to the blue data points in the three panels of Fig. 6. Notice the peak at $\Phi \simeq 0.78$ diminishes with decreasing $L_X$, while the peak at $\Phi \simeq 1.05$ stays relatively constant. This figure covers one revolution of the NS.

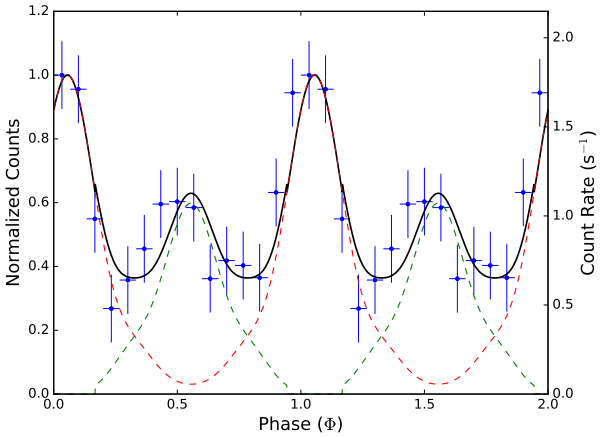


**Figure 8.** The folded profile and *Polestar* fit from the lone *NuSTAR* observation of SXP 1062 (ObsID 90501344002). Despite an increase in luminosity and a significant shortening of the period, the double-peaked signature of this source is still present, yet the peaks are now separated by $\sim 0.5$ Φ.

reported by Serim et al. (2017). The folded pulse profile still exhibits a double-peaked structure as it did before, however the peaks are now separated by nearly a full half-phase (Fig. 8).

Remarkably, despite these changes, the *Polestar* best-fit parameters did not change appreciably from earlier observations, with $i = 80°$ and $\theta = 53°$(see Tables C1 & C2).

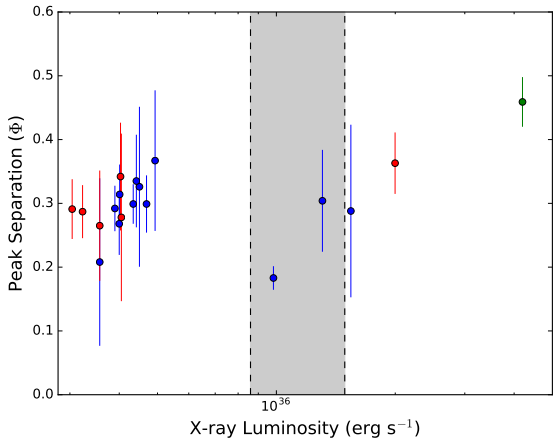


**Figure 9.** Peak separation as a function of X-ray luminosity for all of the pulse profiles in this study. The grey shaded region denotes a range of possible values for $L_{X,crit}$ corresponding to different B-field values given in the literature. As in previous figures, blue denotes *Chandra* data, red denotes *XMM-Newton* data, and green represents *NuSTAR* data.

### 5.4 Peak Separation in the Super-Critical Regime

The double-peaked profiles of SXP 1062 tend to have a peak-separation (defined as the distance in units of phase from the tip of the primary peak to the tip of the secondary peak) on the order of $\sim 0.3$ **Φ** (see Fig. 9).

Five of the nineteen profiles were observed in higher luminosity states, nearing or just following periastron and the associated Type I outburst (see again Fig. 2). Following Eq. 32 in Becker et al. (2012) we have calculated the critical luminosity for SXP 1062 for a range of magnetic field strengths reported in the literature, yielding $0.9 \times 10^{36}$ erg s$^{-1}$ $\leq L_{X,crit} \leq 1.5 \times 10^{36}$ erg s$^{-1}$. These five profiles sit at or above our calculated range for $L_{X,crit}$. As displayed in Fig. 9, for SXP 1062 the peak separation steadily increases with $L_X$ in this super-critical regime. We explore possible explanations for this relationship in § 6.

### 5.5 The Orientation and Geometry of SXP 1062

The best-fit average geometry for SXP 1062 from the 19 *Polestar* fits is with the inclination angle $(i) = 76.5° \pm 2.3°$ and $\theta = 39.7° \pm 8.3°$. A representation of this geometry can be seen in the top panel of Fig. 10, with the resulting profile (corresponding to the parameter values given in Table 2) in the bottom panel.

These best-fit parameters produce a profile that exhibits three peaks per phase. The most narrow peak occurs at **Φ** = 0, 1, 2..., when all of the detected emission is produced by the primary HS and the secondary HS is completely occulted. The other two peaks are formed when the secondary HS comes into view in conjunction with the primary HS moving away from the LOS.

**Table 2.** SXP 1062 Best-fit Parameters

| $i$ | $\sigma_i$ | $\theta$ | $\sigma_\theta$ | $\phi$ | $\sigma_\phi$ | $P_{cos}$ | $\sigma_{cos}$ | $P_{sin}$ | $\sigma_{sin}$ | $P_{rat}$ | $\sigma_{rat}$ |
|---|---|---|---|---|---|---|---|---|---|---|---|
| 77 | 2.3 | 40 | 8.3 | 244 | 82 | 5.7 | 2.1 | 7.4 | 1.7 | 0.8 | 0.1 |

A table of the best *Polestar* fit parameter values for SXP 1062, along with the standard deviation ($\sigma$) of their respective distributions. The values of $i$, $\theta$, and $\phi$ are reported in degrees.

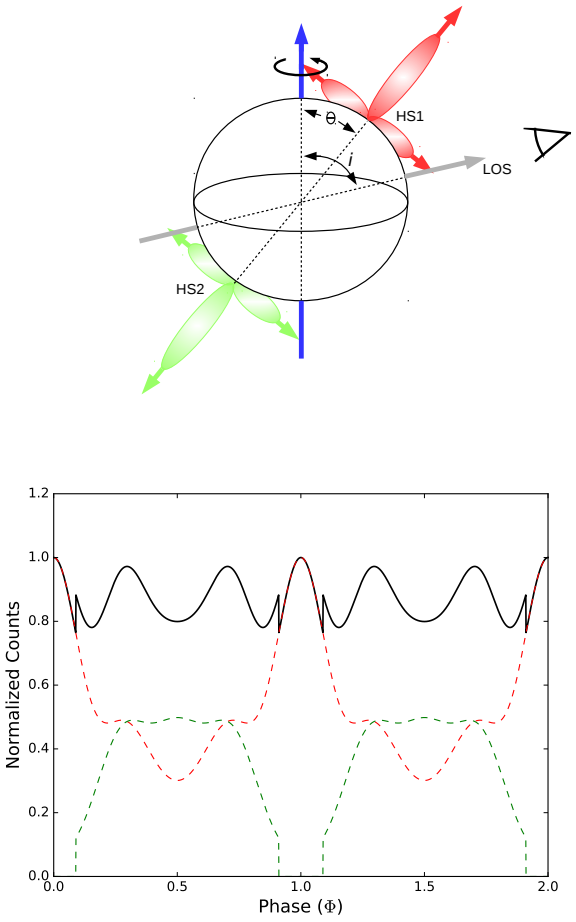


**Figure 10.** The top panel is the average best-fit model for SXP 1062, with $i = 76° \pm 2°$ and $\theta = 40° \pm 9°$. The bottom plot is the *Polestar* profile that corresponds to the best-fit parameters reported in Table 2.

## 6 DISCUSSION

Incorporating the orbital inclination angle calculated by Serim et al. (2017) along with the orientation of the circumstellar disk (Gonzales-Galan et al. 2017) and the inclincation of the NS spin axis derived in this work, a picture of the SXP 1062 system as a whole begins to emerge (see Fig. 11). The angular momentum vector of the NS is almost orthogonal to the angular momentum vector of the Be star, with the NS spin axis nearly parallel to the plane

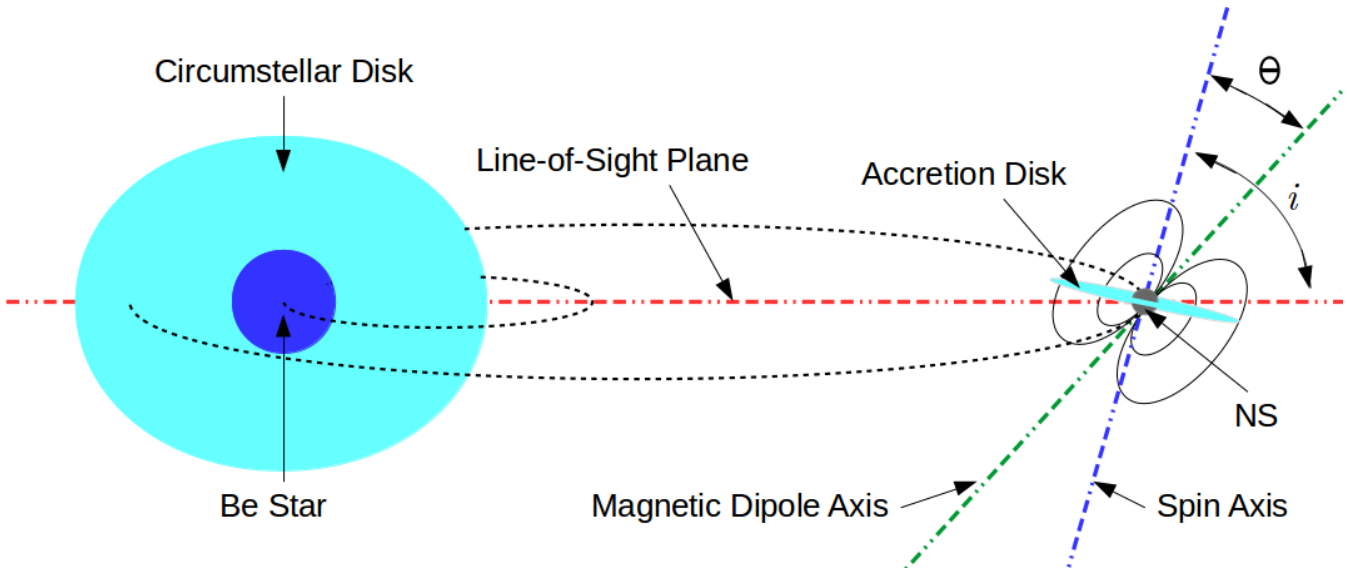


**Figure 11.** A representation of the SXP 1062 system as viewed from earth, not to scale. The orbital inclination angle of 73° is taken from Serim et al. (2017) and the orientation of the circumstellar disk is taken from Gonzales-Galan et al. (2017). The red dashed line represents the plane of the line of sight, the blue dashed line denotes the spin axis, and the green dashed line denotes the magnetic dipole axis. The orbital paths of the NS and the Be star are represented by the black dotted ellipses. The best-fit values of $i$ and $\theta$ from the analysis in this work are 76° and 40°, respectively.

of the circumstellar disk. Likewise the spin axis of the NS is orthogonal to the orbital plane, whereas the spin axis of the Be star is nearly parallel to the orbital plane. This orientation has been proposed for other BeXRB systems, including SXP 5.05 in the SMC (Coe et al. 2015b).

Another strong argument for this particular orientation comes from spectral fitting of the 2014 *Chandra* observations during and after outburst. Gonzales-Galan et al. (2017) determined that the column density increases significantly just prior to periastron, with a subsequent decrease following periastron. This implies that as the NS approaches the Be star it is obscured by the circumstellar disk until periastron occurs, at which point the NS punches through the vertical wall of the disk.

There are multiple possible explanations for the decrease in relative height of the peak at $\Phi \simeq 0.78$ in Fig. 7. One possibility is a transition between accretion regimes (Reig & Milonaki 2016). Perhaps during periastron enough material accretes to form an accretion shock at the magnetic poles, with a column forming below (Becker et al. 2012). Photons emitted from the sides of this column could account for the additional peak separated by one-quarter of a phase from the primary peak. After periastron the X-ray luminosity decreases, as does the volume of accreted matter; the shock recedes closer to the NS surface and the fan component is no longer as productive (Karino 2007).

Another possibility is the secondary peak is evidence of the formation of an accretion curtain. At high accretion rates sheets of declerating plasma follow magnetic field lines to their annular footprints on the NS surface (Miller 1996). In certain regimes, emission from this curtain can dominate the resulting pulse profile, with the shift in phase correlating to the diameter of the emission region.

A third theory involves reflection of energetic photons off the accretion mound that forms at the base of the column (Mushtukov et al. 2018). Again the accretion column would diminish as accretion lessens, leading to fewer photons being reflected from the mound. Similar to the accretion curtain, the spacing of the peaks in the profile is dictated by the extent of the accretion mound on the NS surface.

Fig. 9 displays a trend of increasing peak separation with increasing $L_X$ when SXP 1062 is in the super-critical regime. This relation may be evidence of a secondary pencil beam emitting at an appreciable distance from the magnetic pole. This can occur when photons emitted from the side of the accretion column (i.e. "fan" photons) are directed back down to the NS surface, both by gravity and scattering off relativistic electrons (Truempur et al. 2013).

If this emission mechanism, which has been suggested for other SMC sources (e.g. SMC X-3, see Koliopanos & Vasilopoulos (2018)), occurs in SXP 1062, then the measurement of the peak separation could offer a novel way of determining both the critical luminosity as well as the height of the accretion column. As the column height increases, the photons will travel further transversely before reaching the NS surface, leading to a larger separation between the two pencil beams and consequently a larger separation of the peaks in the pulse profile.

## 7 CONCLUSIONS

We extracted and analyzed 19 individual pulse profiles for the SMC X-ray Pulsar SXP 1062 from *Chandra*, *XMM-Newton*, and *NuSTAR* archival data spanning a decade of observations. Most-likely values for both the inclination angle ($i$) and the angle between the spin and magnetic dipole axes ($\theta$) were determined for this system, with $i = 76^\circ \pm 2^\circ$ and $\theta = 40^\circ \pm 9^\circ$. Additionally changes in the folded pulse profiles at the tail end of a Type I outburst were noted, along with a possible correlation between peak separation and X-ray luminosity in the super-critical regime, where $L_X \geq L_{X,crit}$.

## ACKNOWLEDGEMENTS

This work was facilitated by NASA ADAP grants NNX14-AF77G and 80NSSC18K0430, with UMASS Lowell in conjunction with LoCSST (Lowell Center for Space Science and Technology). The authors would also like to thank J. Hong, H. Klus, and P. Kretschmar for their helpful discussions.

## REFERENCES

Basko, M. M., & Sunyaev, R. A. 1976, MNRAS, 175, 395
Becker, P. A., & Wolff, M. T. 2007, ApJ, 654, 435
Becker, P. A., Klochkov, D., Schonherr, G., et al. 2012, A&A, 544, A123
Bildsten, L., Chakrabarty, D., Chiu, J., et al. 1997, ApJSS, 113, 367
Brown, R. O., Coe, M. J., Ho, W. C. G., & Okazaki, A. T. 2019, MNRAS, 488, 387
Cappallo, R., Laycock, S. G. T., & Christodoulou, D. M. 2017, PASP, 129, 124201
Cappallo, R., Laycock, S. G. T., Christodoulou, D. M., Coe, M. J., & Zezas, A. 2019, MNRAS, 486, 3248
Christodoulou, D. M., Laycock, S. G. T., & Kazanas, D. 2018, MNRAS, 478, 3506
Coe, M. J., Edge, W. R. T., Galache, J. L., & McBride, V. A. 2005, MNRAS, 356, 502
Coe, M. J., Bartlett, E. S., Bird, A. J., et al. 2015, MNRAS, 447, 2387
Coe, M. J., Kirk, J. 2015, MNRAS, 452, 969
Evans, C. J., Howarth, I. D., Irwin, M. J., Burnley, A. W., & Harries, T. J. 2004, MNRAS, 353, 601
Fu, L., & Li, X. 2012, ApJ, 757, 171
Gonzales-Galan, A., Oskinova, L. M., Popov, S. B., et al. 2017, MNRAS, 475, 2809
Haberl, F., Sturm, R., Filipovic, M. D., et al. 2012, A&A, 537, L1
Haschke, R., Grebel, E. K., & Duffau, S. 2012, AJ, 144, 107
Henault-Brunet, V., Oskinova, L. M., Guerrero, M. A., et al. 2012, MNRAS, 420, L13
Ikhsanov, N. R. 2012, MNRAS, 424, L39
Karino, S. 2007, PASJ, 59, 961
Klus, H., Ho, W. C. G., Coe, M. J., Corbet, R. H. D., & Townsend, L. J. 2014, MNRAS, 437, 4
Koliopanos, F., Vasilopoulos, G. 2018, A&A, 614, A23
Laycock, S. 2003, PhD Thesis, University of Southampton
Lipunov, V. M. 1992, *Astrophysics of Neutron Stars*, Springer-Verlag Berlin Heidelberg, ISBN:978-3-642-76352-6
Lomb, N. R. 1976, Ap&SS, 39, 447
Miller, G. S. 1996, ApJ, 468, L29
Mushtukov, A. A., Verhagen, P. A., Tsygankov, S. S., et al. 2018, MNRAS, 474, 5425
Paul, B., Naik, S. 2011, BASI, 39, 429
Popov, S. B., Turolla, R. 2012, MNRAS, 421, L127
Porter, J. M., Rivinius, T. 2003, PASP, 115, 1153
Reig, P., Roche, P. 1999, MNRAS, 306, 100
Reig, P. 2011, Ap&SS, 332, 1
Reig, P., Nespoli, E. 2013, A&A, 551, 17
Reig, P., Milonaki, F. 2016, A& A, 594, A45
Scargle, J. D. 1982, ApJ, 263, 835
Schmidtke, P. C., Cowley, A. P., Udalski, A. 2012, ATel, 4596
Schönherr, G., Wilms, J., Kretschmar, P., et al. 2007, A&A, 472, 353
Serim, M. M., Şahiner, Ş., Çerri-Serim, D., İnam, S. Ç., & Baykal, A. 2017, MNRAS, 471, 4982
Strum, R., Haberl, F., Oskinova, L., et al. 2013, A&A, 556, A139
Truemper, J. E., Dennerl, K., Kylafis, N. D., Ertan, Ü., & Zezas, A. 2013, ApJ, 764, 49
Walter, R., Lutovinov, A. A., Bozzo, E., Tsygankov, S. S. 2015, A&ARv, 23, 2
Yang, J., Laycock, S. G. T., Christodoulou, D. M., et al. 2017, ApJ, 839, 119
Zavlin, V. E., Pavlov, G. G., Shibanov, Y. A., & Ventura, J. 1995, A&A, 297, 441

## APPENDIX A: CALCULATION OF THE PULSED FRACTION

For each profile that was folded on a significant period detection, the pulsed fraction (PF) was calculated following the prescription found in Bildsten et al. (1997). The calculation proceeded as follows:

The mean flux ($\bar{F}$) and the pulsed flux ($F_p$) were calculated for each profile, where:

$$\bar{F} = \int_0^1 F(\phi) d\phi \tag{A1}$$

and

$$F_p = \int_0^1 [F(\phi) - F_{min}] d\phi \tag{A2}$$

with $F_{min} = \min[F(\phi)]$.

The pulsed fraction is then defined as the ratio of the pulsed flux to the mean flux:

$$\mathrm{PF} = \frac{F_p}{\bar{F}} \tag{A3}$$

It should be noted that in the case of a binned profile, the integrals in the first two equations become sums.

**Table B1.** Table of *Polestar* Parameters

| Parameter | Description | Value in this study |
|---|---|---|
| $\theta_{LOS}$ | Latitudinal angle between the line of sight and the NS spin axis | $0^\circ \leq i \leq 90^\circ$ |
| $\phi_{LOS}$ | Longitudinal angle between the line of sight and an arbitrary $\Phi = 0$ latitude | zero |
| $\theta_{HS1}$ | Latitudinal angle between the primary HS vector and the NS spin axis | $0^\circ \leq \theta \leq 90^\circ$ |
| $\phi_{HS1}$ | Longitudinal angle between the primary HS vector and the arbitrary $\Phi = 0$ latitude | $0^\circ \leq \phi \leq 360^\circ$ |
| $\theta_{HS2}$ | Latitudinal angle between the secondary HS vector and the NS spin axis | $180^\circ$- $\theta$ |
| $\phi_{HS2}$ | Longitudinal angle between the secondary HS vector and the arbitrary $\Phi = 0$ latitude | $180^\circ$+ $\phi$ |
| $P_{cos}$ | The power of the cosine emission function (i.e. the width of the pencil beam) | $1 \leq P_{cos} \leq 9$ |
| $P_{sin}$ | The power of the sine emission function (i.e. the width of the fan beam) | $1 \leq P_{sin} \leq 9$ |
| $P_{rat}$ | The fractional contribution from $P_{cos}$ vs. $P_{sin}$ to the overall emission | $0 \leq P_{rat} \leq 1$ |
| $HS_{rat}$ | The fractional contribution from each HS to the overall emission | 0.5 |
| $R_{NS}$ | The radius of the NS | 10 km |
| $M_{NS}$ | The mass of the NS | $1.4 M_\odot$ |

A table listing the twelve free parameters (with brief descriptions) in the version of *Polestar* with two HSs. In the fitting performed for this study six of these parameters remained free (namely $\theta_{LOS}$, $\theta_{HS1}$, $\phi_{HS1}$, $P_{cos}$, $P_{sin}$, and $P_{rat}$). The remaining six were fixed for the fitting at the values given in the right-hand column.

## APPENDIX B: A DISCUSSION ON *Polestar* PARAMETERS

When creating any model and fitting it to data there is an inherent balncing act between maximizing the quality of fit and minimizing the computational requirements. Both generalizations in the model and streamlining of the fitting procedure must be incorporated to perform the operation in a tractable amount of time. *Polestar* (Cappallo et al. 2017) is no exception.

In order to reduce fitting time *Polestar* incorporates a modified coordinate descent algorithm (see § 3.1 in Cappallo et al. (2019) for a discussion on this technique). Similarly, the model itself was simplified for the fitting performed in this study. A version of *Polestar* with two HSs was used (simulating a magnetic dipole field), with a maximum of twelve free parameters, as listed in Table B1. The computation time for fitting a large data set with a twelve-parameter model was still untenable, so more simplifications had to be incorporated.

To this end an antipodal configuration was adhered to, where both HS vectors point along the magnetic dipole axis, which itself passes through the center of the NS. This decision automatically fixes the location of the secondary HS (defined by $\theta_{HS2}$ and $\phi_{HS2}$) in relation to the primary HS (i.e. $\theta_{HS2}$ = 180°- $\theta_{HS1}$ and $\phi_{HS2}$ = 180°+ $\phi_{HS1}$). Additionally, the radius of the NS ($R_{NS}$) and the mass of the NS ($M_{NS}$) were both fixed at the canonical values of 10 km and $1.4 M_\odot$, respectively. Similarly the ratio of each HS's contribution to the overall emission ($HS_{rat}$) was fixed at a value of 0.5 (i.e. both HSs emit at identical intesities). Combined these simplifications reduced the space of states (and thus the computation time) by a factor of order $10^5$.

It should be noted that a slight deviation from an antipodal arrangement can be acomplished with just one additional parameter, namely an angle ($\xi_{HS2}$) defining the position of the secondary HS with respect to the magnetic axis (more precisely, one extra angle defines a circle on which the secondary HS must sit). While this does allow for greater complexity in the resulting pulse profiles, assuming the angle is small ($\xi_{HS2} \leq 10^\circ$), it does not lead to a marked change for the results reported in this study (e.g. the distributions of $i$ and $\theta$ show little deviation from those presented in Fig. 5). Thus the conclusions presented in this paper are robust to this added complexity.

## APPENDIX C: FITTING TABLES

This paper has been typeset from a TEX/LATEX file prepared by the author.

**Table C1.** SXP 1062 - 6-parameter *Polestar* fit.

| ID | $i$ | $\theta$ | $\phi$ | $P_{cos}$ | $P_{sin}$ | $P_{rat}$ | $\chi^2$ |
|---|---|---|---|---|---|---|---|
| 602520401 | 74 | 33 | 200 | 6 | 7 | 0.7 | 2.38 |
| 602520201 | 76 | 33 | 112 | 5 | 9 | 0.7 | 5.03 |
| 12130 | 78 | 29 | 224 | 9 | 7 | 0.8 | 4.22 |
| 602520301 | 74 | 39 | 228 | 7 | 9 | 0.7 | 7.88 |
| 12131 | 81 | 55 | 348 | 6 | 6 | 0.8 | 13.74 |
| 12134 | 81 | 37 | 352 | 7 | 2 | 0.9 | 5.29 |
| 10986 | 77 | 39 | 212 | 3 | 8 | 0.6 | 4.23 |
| 11979 | 61 | 63 | 188 | 1 | 5 | 0.7 | 6.79 |
| 602520501 | 77 | 33 | 228 | 5 | 9 | 0.7 | 5.45 |
| 11978 | 75 | 35 | 92 | 9 | 7 | 0.8 | 4.65 |
| 11988 | 73 | 41 | 136 | 3 | 7 | 0.6 | 11.56 |
| 11989 | 74 | 51 | 336 | 4 | 8 | 0.8 | 8.6 |
| 12207 | 76 | 45 | 232 | 2 | 9 | 0.5 | 15.72 |
| 700381801 | 61 | 31 | 340 | 5 | 5 | 0.8 | 0.65 |
| 721960101 | 75 | 33 | 184 | 8 | 7 | 0.8 | 2.82 |
| 15785 | 75 | 45 | 336 | 6 | 7 | 0.8 | 10.52 |
| 15786 | 75 | 33 | 208 | 8 | 9 | 0.8 | 4.48 |
| 15787 | 77 | 55 | 332 | 3 | 9 | 0.8 | 2.74 |
| 90501344002 | 80 | 53 | 340 | 4 | 9 | 0.9 | 6.05 |
| mean $\pm$ $\sigma$ | 75 $\pm$ 6 | 41 $\pm$ 10 | 244 $\pm$ 83 | 5 $\pm$ 2 | 7 $\pm$ 2 | 0.7 $\pm$ 0.1 | 6.46 $\pm$ 3.89 |

SXP 1062 pulse profiles fitted with 6-parameter *Polestar*, presented in chronological order. The columns are Observation ID, the inclination angle ($0^\circ \leq i \leq 90^\circ$), the angle between the primary hot spot and the spin axis ($0^\circ \leq \theta \leq 90^\circ$), the angle between the primary hot spot and an (arbitrary) phase = 0 point ($0^\circ \leq \phi \leq 360^\circ$), the power of the cosine beaming function ($1 \leq P_{cos} \leq 9$), the power of the sine beaming function ($1 \leq P_{sin} \leq 9$), the ratio between the cosine and sine beaming functions ($0 \leq P_{rat} \leq 1$), and the corresponding chi-squared statistic value ($\chi^2$). The final row gives the mean $\pm$ the standard deviation ($\sigma$) for each distribution. All angles are given in units of degrees.

**Table C2.** SXP 1062 - 6-parameter *Polestar* fit with $i = 75^\circ \pm 6^\circ$.

| ID | $i$ | $\theta$ | $\phi$ | $P_{cos}$ | $P_{sin}$ | $P_{rat}$ | $\chi^2$ |
|---|---|---|---|---|---|---|---|
| 602520401 | 74 | 33 | 200 | 6 | 7 | 0.7 | 2.38 |
| 602520201 | 76 | 33 | 112 | 5 | 9 | 0.7 | 5.03 |
| 12130 | 78 | 29 | 224 | 9 | 7 | 0.8 | 4.22 |
| 602520301 | 74 | 39 | 228 | 7 | 9 | 0.7 | 7.88 |
| 12131 | 81 | 55 | 348 | 6 | 6 | 0.8 | 13.74 |
| 12134 | 81 | 37 | 352 | 7 | 2 | 0.9 | 5.29 |
| 10986 | 77 | 39 | 212 | 3 | 8 | 0.6 | 4.23 |
| 11979 | 77 | 37 | 196 | 6 | 7 | 0.7 | 7.54 |
| 602520501 | 77 | 33 | 228 | 5 | 9 | 0.7 | 5.45 |
| 11978 | 75 | 35 | 92 | 9 | 7 | 0.8 | 4.65 |
| 11988 | 73 | 41 | 136 | 3 | 7 | 0.6 | 11.56 |
| 11989 | 74 | 51 | 336 | 4 | 8 | 0.8 | 8.6 |
| 12207 | 76 | 45 | 232 | 2 | 9 | 0.5 | 15.72 |
| 700381801 | 79 | 29 | 336 | 7 | 5 | 0.9 | 0.85 |
| 721960101 | 75 | 33 | 184 | 8 | 7 | 0.8 | 2.82 |
| 15785 | 75 | 45 | 336 | 6 | 7 | 0.8 | 10.52 |
| 15786 | 75 | 33 | 208 | 8 | 9 | 0.8 | 4.48 |
| 15787 | 77 | 55 | 332 | 3 | 9 | 0.8 | 2.74 |
| 90501344002 | 80 | 53 | 340 | 4 | 9 | 0.9 | 6.05 |
| mean $\pm$ $\sigma$ | 77 $\pm$ 2 | 40 $\pm$ 8 | 244 $\pm$ 82 | 6 $\pm$ 2 | 7 $\pm$ 2 | 0.8 $\pm$ 0.1 | 6.51 $\pm$ 3.88 |

SXP 1062 pulse profiles fitted with 6-parameter *Polestar* with $i$ fixed at $75^\circ \pm 5^\circ$, presented in chronological order. The columns are Observation ID, the inclination angle ($70^\circ \leq i \leq 80^\circ$), the angle between the primary hot spot and the spin axis ($0^\circ \leq \theta \leq 90^\circ$), the angle between the primary hot spot and an (arbitrary) phase = 0 point ($0^\circ \leq \phi \leq 360^\circ$), the power of the cosine beaming function ($1 \leq P_{cos} \leq 9$), the power of the sine beaming function ($1 \leq P_{sin} \leq 9$), the ratio between the cosine and sine beaming functions ($0 \leq P_{rat} \leq 1$), and the corresponding chi-squared statistic value ($\chi^2$). The final row gives the mean $\pm$ the standard deviation ($\sigma$) for each distribution. All angles are given in units of degrees.